

## Haiyang He

Department of Mechanical and Industrial Engineering,  
2039 Engineering Research Facility,  
University of Illinois at Chicago,  
842 W. Taylor Street,  
Chicago, IL 60607  
e-mail: Hhe20@uic.edu

## Jie Xu

Mem. ASME  
Department of Mechanical and Industrial Engineering,  
2039 Engineering Research Facility,  
University of Illinois at Chicago,  
842 W. Taylor Street,  
Chicago, IL 60607  
e-mail: jixu@uic.edu

## Xiaoming Yu

Mem. ASME  
College of Optics & Photonics,  
University of Central Florida CREOL,  
4304 Scorpius Street,  
Orlando, FL 32816-2700  
e-mail: yux@creol.ucf.edu

## Yayue Pan<sup>1</sup>

Mem. ASME  
Department of Mechanical and Industrial Engineering,  
2039 Engineering Research Facility,  
University of Illinois at Chicago,  
842 W. Taylor Street,  
Chicago, IL 60607  
e-mail: yayuepan@uic.edu

# Effect of Constrained Surface Texturing on Separation Force in Projection Stereolithography

*In projection stereolithography (SL) processes, the separation of a newly cured layer from the constrained surface is a historical technical barrier and still greatly limits its printable size, process reliability, and print speed. This paper presents an approach to reduce the separation force in projection SL processes by texturing the constrained surface with radial microgroove patterns. Separation forces with conventional smooth constrained surface and textured surface are both modeled. The analytical model suggests that a proper design of micropatterns of the constrained surface is capable of reducing separation forces greatly. Furthermore, a projection SL testbed with online separation force monitoring unit is developed for experimental study. Experimental results verified the effectiveness of microsurface textures in reducing separation forces. Test cases also show that with the help of the proposed textured constrained surface, parts with wide solid cross sections that could not be printed using conventional methods were manufactured successfully. The influence of the textured constrained surface on the printed parts' surface roughness is studied, a gray scale projection approach is proposed to eliminate the influence and improve the surface quality of printed parts. Hence, the presented methods can help to improve the manufacturing capability of Projection SL processes.*

[DOI: 10.1115/1.4040322]

## 1 Introduction

Projection stereolithography (SL) is one of the most important additive manufacturing technologies currently available and also the first commercialized additive manufacturing technology. In projection SL process, liquid photosensitive polymer is cured usually through the use of a digital light processing (DLP) projector, which supplies the amount of energy via projecting digital mask images to induce a curing reaction, forming a highly cross-linked polymer [1]. Compared to other polymer additive manufacturing techniques like extrusion or jetting processes, projection SL produces parts with the highest accuracy and the best surface finish.

There are two ways to cure liquid polymer in projection SL, free surface method and constrained surface method, as illustrated in Fig. 1. Compared to free surface process, the constrained surface process has several advantages including less material waste, higher resolution, and faster speed, and is being used increasingly recently [2–9]. Despite the advantages, the separation of a newly cured layer from the constrained surface is a historical technical barrier and still greatly limits the printable size, process reliability, and print speed [10]. Manufacturing defects and failures caused by over-large separation force in SL processes include holes in printed parts, adhesion of cured layers on constrained surface,

separate layers, failed parts, and broken constrained surface. Some examples are shown in Fig. 2.

As illustrated in Fig. 1, in constrained surface projection SL process, the separation force occurs in the process of lifting newly cured layer up and refilling liquid resin into the gap created during lifting process. Hence, the separation force exerted on newly cured layer is actually the suction force caused by pressure difference in liquid filling [11,12].

Extensive research has been conducted to study and reduce separation forces [13–16]. Approaches like peeling, two-way movement, and coating have been developed. However, these

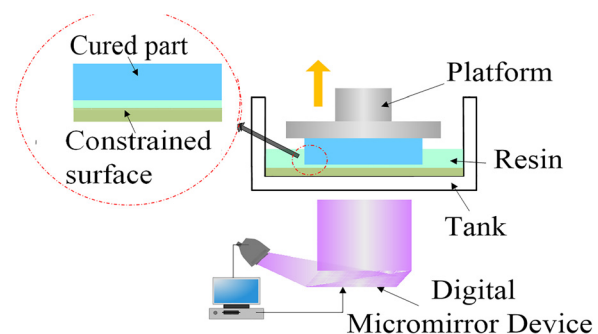


**Fig. 1** A schematic diagram of constrained surface based Projection SL

<sup>1</sup>Corresponding author.

Manuscript received October 13, 2017; final manuscript received May 11, 2018; published online June 28, 2018. Assoc. Editor: Qiang Huang.

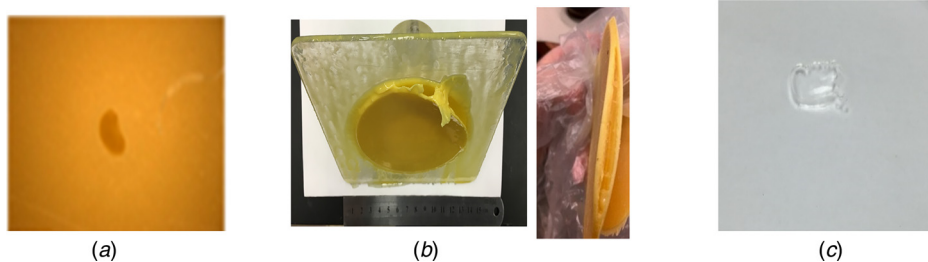


**Fig. 2 Manufacturing failures and defects caused by over-large separation force: (a) holes on printed surface; (b) separate layers; and (c) broken film, which is functioning as the constrained surface**

approaches may prolong the total build time, require much larger liquid tank, and frequent replacements of coatings [17,18]. The peeling approach introduces other problems like corrugated constrained surfaces and large peeling force [19,20]. These drawbacks are more significant when the print area is large solid cross section. Hence separation problem still remains to be the primary challenge and limits the manufacturing capability of projection SL. For example, the building envelopes of current projection SL machines are all in inch level and no greater than  $8 L \times 5 W \times 10 H$ . As a result, to produce a part in feet level is almost impossible. Therefore, it is of high significance to reduce the separation force and enhance the capability of projection SL.

Against this background, this paper aims to develop novel approaches to reducing separation forces, without sacrificing other properties like speed, volume, and reliability. A constrained surface texturing approach for separation force reduction is developed in this study.

## 2 Effects of Constrained Surface Texture on Separation Force

In constrained surface SL, conditions of the interfaces, the newly cured layer surface and constrained surface, play important roles in determining separation forces. In addition, surface texturing has been widely used for altering pressure gradient or liquid flow dynamics in various applications [21–24], but not yet in constrained surface design for stereolithography. Hence, in this study, we investigate how to modify the constrained surface to reduce separation forces in SL process.

Figure 3(a) shows a schematic diagram of the separation area in conventional projection SL systems based on smooth constrained surface.  $R$  is the radius of the part, and  $h$  is the height of the gap between the newly cured layer and the coating. Figure 3(b) is a schematic of separation area with proposed constrained surface, which is patterned with a radial microgroove pattern. The radial microgroove pattern was designed and implemented for reducing separation force as well as assisting liquid resin refilling, which will not only extend the capability of conventional layer by layer printing but also benefit continuous printing. The microgroove

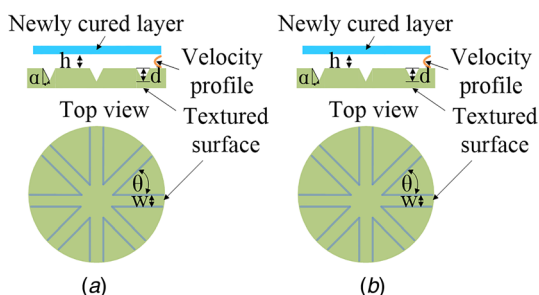


**Fig. 3 Schematic of separation areas with a solid circular layer and (a) nontextured constrained surface and (b) textured constrained surface**

pattern has four design parameters: groove width  $w$ , groove depth  $d$ , the number of grooves is  $n$ , and groove radial distance  $\theta$ .

To investigate effects of surface texture on separation forces and learn how to design parameters, the liquid filling process and separation force are modeled for both conventional smooth surface and textured surface.

### 2.1 Separation Force With Smooth Constrained Surface.

Given Navier–Stokes equation  $\mu(\partial^2 u / \partial z^2) = (dP/dr)$ , the flow velocity profile could be obtained by integrating both sides and applying boundary conditions

$$u = \frac{1}{2\mu} \frac{dP}{dr} (Z^2 - Z \cdot h) \quad (1)$$

where  $\mu$  is the viscosity of the liquid. Based on mass conservation principle, the relationship between the  $Z$ -stage moving speed  $V$  and liquid flow rate  $Q$  can be found

$$Q = V \cdot \pi \cdot r^2 = 2 \cdot \pi \cdot r \int_0^h u dz \quad (2)$$

By substituting Eq. (1) into Eq. (2), the pressure gradient  $\nabla P$  and resulted pressure  $P$  could be derived as

$$\nabla P = \frac{dP}{dr} = -V\mu r \cdot \frac{6}{h^3} \quad (3)$$

Integrating both sides of Eq. 3 with respect to  $r$  and applying the boundary condition  $r = R, P = 0$ , we can get

$$P = -\frac{3\mu V}{h^3} \cdot r^2 + \frac{3\mu V}{h^3} \cdot R^2 \quad (4)$$

Thus, the separation force  $F$  exerted on part can be calculated by integrating the pressure across the area

$$F = \int_0^R 2\pi r P dr = \frac{3\pi \cdot \mu V}{2 \cdot h^3} \cdot R^4 \quad (5)$$

The separation force model  $F$  reveals that the separation force grows fast as the size of the cross-sectional area of the printing part increases. In addition, the resin viscosity and the manufacturing speed also have an impact on the separation force.

### 2.2 Separation Force With Textured Constrained Surface.

According to Ref. [25], the hydraulic resistance  $R_{hyd}$  for straight channels with arbitrary cross-sectional shape could be approximated by

$$R_{hyd} \approx 2 \cdot \mu \cdot L \cdot \frac{Pe^2}{A^3} \quad (6)$$

where  $L$  is the channel length,  $\mu$  is the dynamic viscosity of the liquid,  $A$  is the cross-sectional area, and  $Pe$  is the perimeter. Also, by definition, the hydraulic resistance is

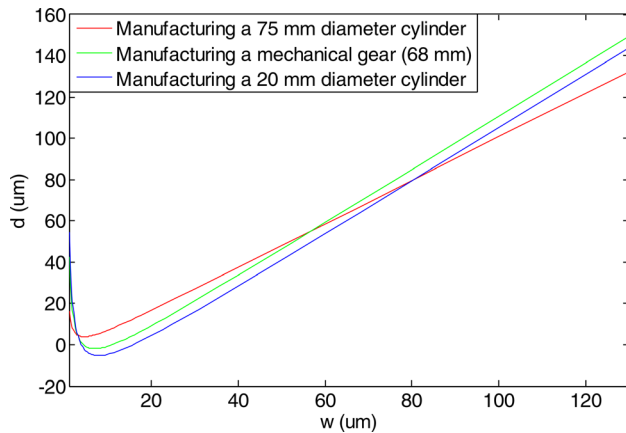


Fig. 4 The relationship between width and depth of microtextures for achieving the smallest separation force

$$R_{\text{hyd}}(\Delta P) \equiv \frac{\Delta P}{Q(\Delta P)} \quad (7)$$

where  $\Delta P$  is a certain pressure drop and  $Q$  is the flow rate.

From Eqs. (6) and (7), we can obtain  $\Delta P/L = 2 \cdot \mu \cdot Q(\Delta P) \cdot (\text{Pe}^2/A^3)$ . Thus, the pressure gradient for channel length  $dr$  along the radius is

$$\nabla P = \frac{dP}{dr} = Q \cdot 2\mu \cdot \frac{\text{Pe}^2}{A^3} \quad (8)$$

For situation with microtextures

$$\text{Pe} = 2 \cdot 2\pi \cdot r + 2 \cdot n \cdot \left( \frac{d}{\cos(\alpha/2)} - \frac{w}{2} \right) \quad (9)$$

$$A = 2\pi \cdot r \cdot h + 0.5n \cdot w \cdot d \quad (10)$$

$$Q = V \cdot \pi \cdot r^2 \quad (11)$$

where  $V$  is the separation speed,  $n$  is the number of grooves,  $w$  and  $d$  are the width and depth of the grooves, and  $h$  denotes the height of the gap.

By substituting Eqs. (9)–(11) into Eq. (8), we can obtain

$$\nabla P = \frac{dP}{dr} = V \cdot \pi r^2 \cdot 2\mu \cdot \frac{\left( 2 \cdot 2\pi \cdot r + 2 \cdot n \cdot \left( \frac{d}{\cos(\alpha/2)} - \frac{w}{2} \right) \right)^2}{(2\pi \cdot r \cdot h + 0.5n \cdot w \cdot d)^3} \quad (12)$$

$$\frac{\partial \nabla P}{\partial w} = 2\mu V \pi r^2 \frac{\left[ -2n \left( 4\pi r + \frac{2nd}{\cos(\alpha/2)} - nw \right) (2\pi rh + 0.5ndw) - 1.5nd \left( 4\pi r + \frac{2nd}{\cos(\alpha/2)} - nw \right)^2 \right]}{(2\pi rh + nwd)^4} \quad (13)$$

Since  $w$ ,  $d$ ,  $n$  and  $h$  are all larger than zero and  $4\pi r \gg nw$ , above equation cannot be zero.

Similarly, take the partial derivative of the pressure gradient with respect to  $d$  in Eq. (12),

$$\frac{\partial \nabla P}{\partial d} = 2\mu V \pi r^2 \frac{\frac{4n}{\cos(\alpha/2)} \left( 4\pi r + \frac{2nd}{\cos(\alpha/2)} - nw \right) (2\pi rh + 0.5nwd) - 1.5nw \left( 4\pi r + \frac{2nd}{\cos(\alpha/2)} - nw \right)^2}{(2\pi rh + nwd)^4} \quad (14)$$

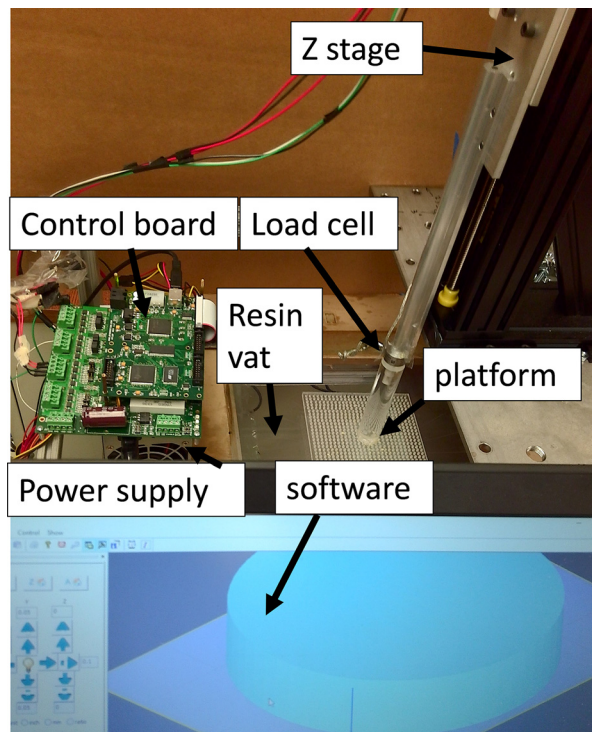


Fig. 5 Hardware setup

By taking integral of the pressure  $P$  on each unit circle, the separation force could be calculated. To investigate the effects of microgrooves on separation force reduction, pressure gradient is calculated for textured surface using Eq. (12), and then compared with pressure gradient for smooth surface in Eq. (3). It was found that textured surface will reduce pressure gradient by  $\sim 60\%$  compared with conventional smooth surface when other conditions are restricted the same and hence smaller separation force than those of smooth polydimethylsiloxane (PDMS).

To achieve the smallest separation force, the pressure  $P$  should be the lowest. Based on Eq. 12 and its derivative with respect to  $r$ , it could be found that pressure  $P$  is a convex function of  $r$ . Therefore, when  $r$  is in the domain of  $(0, R]$ ,  $P$  is the lowest when the pressure gradient  $\nabla P = (dP/dr)$  is the smallest. It can also be seen that  $\nabla P$  is a convex function of  $w$  and  $d$ . Thus, when other conditions are fixed, to achieve the smallest pressure gradient, taking the partial derivative of the pressure gradient with respect to  $w$  in Eq. (12), we can get

Set  $\partial \nabla P / \partial d = 0$

$$d = \frac{16\pi rh + 3nw^2 \cos(\alpha/2) - 12\pi rw \cos(\alpha/2)}{2nw} \quad (15)$$

Therefore, the microtexture height and width,  $d$  and  $w$ , should be designed based on the relationship described in Eq. (15) for achieving the smallest separation force.

Based on the study in Ref. [26–30], the oxygen inhibition layer thickness above a PDMS film is  $\sim 2 \mu\text{m}$ . Thus, when  $h$  is fixed at  $2 \mu\text{m}$ , the relationship between the width and depth of the microtextures is shown in Fig. 4. The aforementioned relationship can be used as a guide when designing the parameters of the textures on PDMS.

### 3 Textured Constrained Surface Based Projection Stereolithography Experimental Setup

As shown in Fig. 5, a constrained surface based projection SL testbed was built. The setup consists of an imaging unit, a resin vat, a linear actuator that elevates the build platform, a control board, and a load cell that measures the separation force. A load cell from FUTEK (Irvine, CA) was mounted directly on the platform, so real-time force can be measured and recorded. An off-the-shelf DLP projector was used as the imaging unit. The optical lenses of the projector were modified to reduce the projection distance. The light source was a 405 nm UV projector, which gave a focused image size of  $128.97 \text{ mm} \times 96.44 \text{ mm}$  and a resolution of  $1920 \times 1080$ . The DLP chip used was DLP6500FLQ from Texas Instruments (Dallas, TX). It has a high-resolution array with over 2 million micromirrors. The micromirror pitch is  $7.56 \mu\text{m}$ . Various projection settings, including focus, key stone rectification, brightness, and contrast were adjusted to achieve a sharp projection image on the projection plane. The resin vat was made with Acrylic. PDMS film was coated on the bottom of the resin vat by mixing the base polymer with curing agent with a 10 to 1 weight ratio and microtextures were generated on the coated PDMS film directly using the laser micromachining approach discussed in Sec. 4.1. A precision position stage from Velmex was used as the linear actuator that drives the platform along Z axis. A six-axis motion control board from DYNAMOTION was implemented to control the Z-stage motion, light projection and to synchronize the motion and projection. A process control testbed was developed using C++ language. It integrated the geometry slicing, image projection, and motion controlling. In addition, an online force monitoring testbed was developed in MATLAB. It reads and processes data from the load cell, and saves the separation force in real time.

Conventional projection SL systems are usually based on smooth PDMS films or smooth TEFLON films. In this study, PDMS films were prepared and coated on bottom surfaces of the resin vat. To explore the potential of textured constrained surface in reducing separation forces, both conventional smooth PDMS films, and PDMS films with designed surface textures were tested.

For comparison, a commercial DLP 3D printer from Envision-TEC (Dearborn, MI) was also tested in the experiment. As described in the specs of the printer, the light source of this

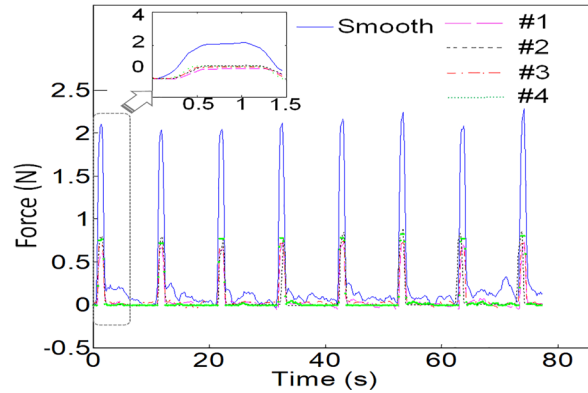


Fig. 7 Separation forces during printing 8 layers by using non-textured PDMS film and the four textured PDMS films showed in Fig. 6

commercial 3D printer is a UV light projector, which produces projection image with a resolution of  $1024 \times 768$  and a full image size of  $100.26 \text{ mm} \times 75.25 \text{ mm}$ . A layer thickness of  $50 \mu\text{m}$  was used in all tests.

## 4 Experimental Results and Discussions

### 4.1 Polydimethylsiloxane Texturing and Force Measurements.

Figure 3(b) is an illustration of the resin replenishment with a textured surface, where the constrained surface is patterned with radially symmetric microgrooves. Those microgrooves will help increase the flow pathway cross section, hence the resin flow rate. Micropatterns with different parameter settings, i.e., width and depth of the microgrooves, number of grooves, have been prepared on 1 mm thick PDMS substrates.

To generate microgrooves on PDMS, a conventional 1 mm smooth PDMS film was first coated on the bottom of the resin vat by mixing the base polymer with curing agent with a 10 to 1 weight ratio. After the PDMS coating was ready, designed micropatterns were sent to a laser machine. By adjusting the laser parameters such as scanning speed and power, various geometries of microgrooves could be fabricated on the PDMS coating.

Microscopic images of the top view of four samples are shown in Fig. 6, where the gray scale bar is 0.2 mm. Surface #1 was textured by an acrylic mold fabricated by a micromilling process, consisting of 8 radially symmetrical microgrooves, with  $80 \mu\text{m}$  width and  $80 \mu\text{m}$  depth. The other three surfaces were textured by using femtosecond (fs) laser micromachining technology, which utilized a 40-fs laser beam to fabricate the designed microgrooves with high precision. Details of the laser micromachining process can be found in Ref. [31]. The geometries of the microgrooves in these three samples are: #2-width  $43 \mu\text{m}$ , depth  $46 \mu\text{m}$ , angle  $15 \text{ deg}$ ; #3-width  $60 \mu\text{m}$ , depth  $107 \mu\text{m}$ , angle  $15 \text{ deg}$ ; #4-width  $66 \mu\text{m}$ , depth  $290 \mu\text{m}$ , angle  $15 \text{ deg}$ . It was found that laser micromachining produces PDMS surface textures with a higher accuracy and shape fidelity than the micromilling process. Hence, in

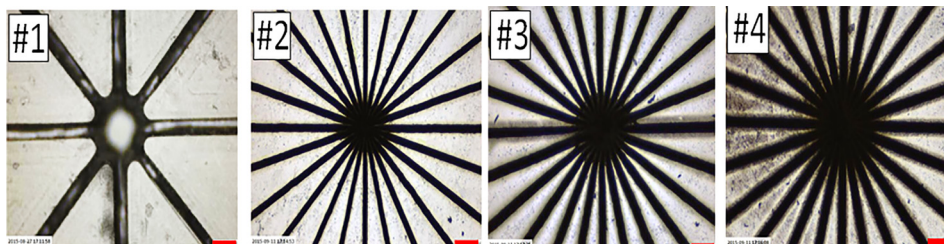


Fig. 6 Microscopic images of four textured surfaces. Scale bar: 0.2 mm.

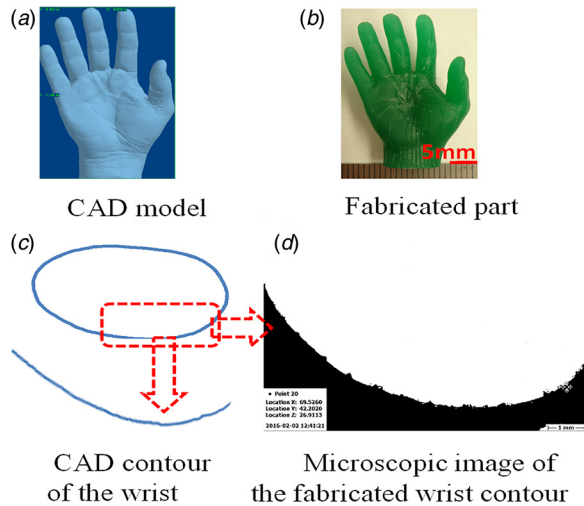


Fig. 8 A hand model printed with textured constrained surface

this paper, the laser micromachining technique was used for PDMS surface texturing in all following experiments.

Experiments were carried out to test the effectiveness of micro-textures on separation force reduction. A solid cylinder with a radius of 10 mm has been built with the conventional projection SL based on smooth constrained surface, and also with the proposed projection SL based on the textured surface (#2-width  $43\ \mu\text{m}$ , depth  $46\ \mu\text{m}$ ) as shown in Fig. 6. In all experiments, a velocity of Z elevator of  $1.56\ \text{mm}^2/\text{s}$  an acceleration of Z elevator of  $1.25\ \text{mm}^2/\text{s}$ , and a layer thickness of  $203.2\ \mu\text{m}$  are used. In addition, the same resin MakerJuice G+ with a viscosity of  $90\ \text{cP}$  is used in all tests.

Forces during printing in the developed SL testbed, with the two types of constrained surfaces, conventional smooth PDMS and textured PDMS surfaces, are measured. Figure 7 plots forces in the process of printing eight successive layers by using smooth surface and the four textured surface samples in Fig. 6. Compared to the conventional smooth PDMS surface, separation forces in the printing process are reduced by  $\sim 60\%$  by using textured surfaces.

Note that the PDMS surface also deforms in the separation processes. Hence, the peak of separation force does not occur

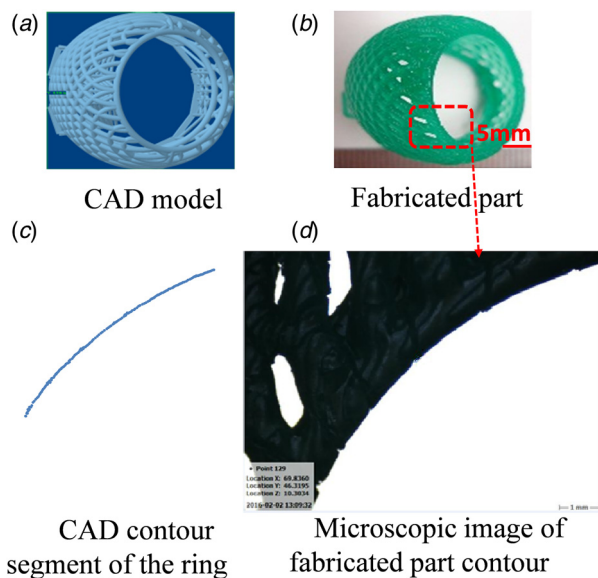


Fig. 9 A ring model printed with textured constrained surface

exactly in the initial moment of part elevation, and the actual separation velocity  $V$  is smaller than the Z-stage velocity due to the deformation of PDMS surface. The experimental results verified that the separation force could be reduced greatly by modifying the constrained surface with radial microgroove textures.

**4.2 Test Case 1: Fabrication of a Hand Model.** The effectiveness of textured surface on reducing separation forces were verified by comparing measured separation forces. To further validate the capability of projection SL based on textured surfaces, multiple complicated structures have been fabricated using the developed testbed and textured surface sample #2. A hand model was printed using proposed approach. Its computer-aided design (CAD) model, fabricated picture, cross-sectional contour and the corresponding microscopic image are shown in Fig. 8. The scale bar is 5 mm.

As shown in the microscopic images, little dents could be identified on the boundaries. It can be explained by the curing depth/width difference between the inner region and boundary, and the liquid depth difference between the microgroove region and the nontextured region. The mask image is binary, consisting of pixels with either full or zero light intensities. Due to light blending, the pixels on boundary receive less light energy than the energy received by pixels in inner regions. Hence, within the same projection time, smaller curing depth/width will be resulted in boundary pixels. Moreover, groove regions have deeper liquid resin. Therefore, with a smaller curing depth/width in boundary while bigger liquid depth in groove region, liquid resin in boundary groove region pixels cannot be fully cured, resulting in little dents on the boundary of the parts. To solve this problem, a grayscale image could be used to tune the curing depth/width in different regions, making uniform curing across the groove area and non-groove areas.

**4.3 Test Case 2: Fabrication of a Ring Model.** To validate the capability of the proposed approach for manufacturing parts with delicate features, a ring model is printed using textured sample #2. Its CAD model, fabricated picture, cross-sectional contour and the corresponding microscopic image are shown in Fig. 9. The scale bar is 5 mm.

Although the conventional smooth PDMS surface can also print such parts of this size, the separation force will be much larger than that of textured PDMS, which will result in shorter life of the constrained surface. As the building size increases, there is a high risk that the increasing separation force will damage the parts or even fail the build process.

**4.4 Test Case 3: Textured Constrained Surface for Fabrication of Different Sizes.** As introduced in Sec. 1, large separation force induced by big cross-sectional size of the printed part usually causes damages to both the newly cured layer and the

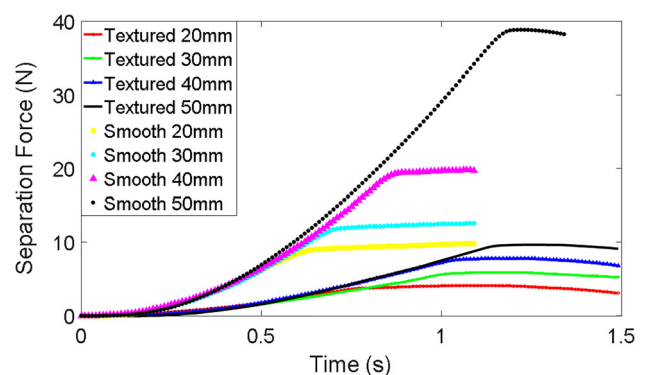


Fig. 10 Separation force for fabricating cylinders with different sizes using textured and smooth constrained surface

constrained surface. It is also indicated by the theoretical models that the separation force would increase as the printing cross-sectional size increases. To test the effectiveness of the proposed textured constrained surface, cylinders with different diameters were printed with both conventional constrained surface and the proposed textured constrained surface. The width and depth of microgrooves on the textured constrained surface were designed according to the theoretical model in Eq. (15) and manufactured to be  $105\ \mu\text{m}$  and  $119\ \mu\text{m}$ , respectively, the number of grooves was 24 (intergroove angle 15 deg). The materials used was G+ from MakerJuice Labs and the diameters of the cylinders were 20 mm, 30 mm, 40 mm, and 50 mm. Separation forces for those different fabrication sizes were recorded and plotted in Fig. 10. For clear demonstration, only a half cycle of the separation force was plotted for each test case.

It can be seen from Fig. 10 that the separation force reached its peak earlier when the printing cross-sectional size is smaller. It is because that the separation time is shorter when the printing cross-sectional size is smaller. In addition, it can be seen from Fig. 10 that the separation force increased dramatically as the cross-sectional size of the part increased, when the conventional smooth constrained surface is used. The peak separation force reached  $\sim 40\ \text{N}$  during the process of printing a 50 mm diameter cylinder. However, when a textured constrained surface was used, the separation force grew slightly with the fabrication size. It verified the effectiveness of the proposed textured constrained surface in reducing the separation force and fabricating parts with different sizes.

**4.5 Test Case 4: Fabrication of a 75 mm Diameter Cylinder.** Printing geometry with a wide solid cross section has always been a challenge for constrained surface SL due to over-large separation force. To validate the effectiveness of textured surface, PDMS constrained surface on fabricating objects with wide solid cross sections with small separation force, a 75 mm diameter cylinder, was tested. The height of the cylinder is 25 mm.

The material used for experiments was G+ (green) from MakerJuice Labs. The layer thickness was set to be  $50\ \mu\text{m}$ . The part was printed both in a commercial machine, MicroEDU from EnvisionTEC (Dearborn, MI), with a smooth constrained surface provided from the company, and our prototype with textured constrained surface. According to the theoretical model in Eq. (15), the constrained surface was textured with microgrooves with a  $105\ \mu\text{m}$  width,  $119\ \mu\text{m}$  depth, and a 15 deg intergroove angle. The process settings in the commercial machine were the default optimal settings given by the machine. With the commercial machine, the part failed during the printing process at around 1 mm in height. The failed part is shown in Fig. 11(a). However, with the textured constrained surface, the printing job was successfully completed and the printed part is shown in Fig. 11(b). The process settings, including projection image size, light

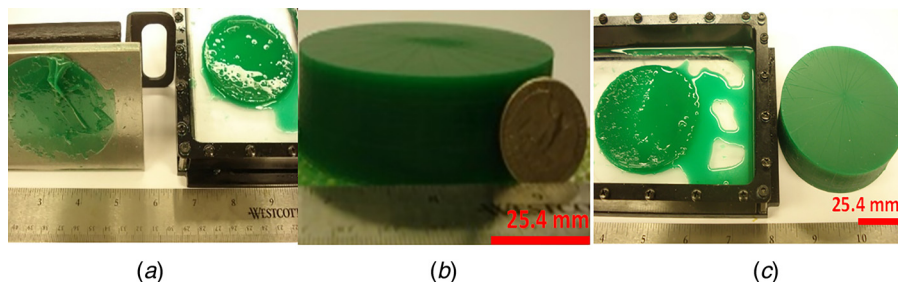


Fig. 11 (a) Failure of printing a 75 mm diameter cylinder using a commercial machine. Part was pulled down from the platform due to over-large separation force and stick on the constrained surface, (b) success of printing a 75 mm cylinder using a textured constrained surface based testbed, and (c) comparison between the failed part stick on the constrained surface of the commercial machine and successfully printed part using the textured constrained surface.

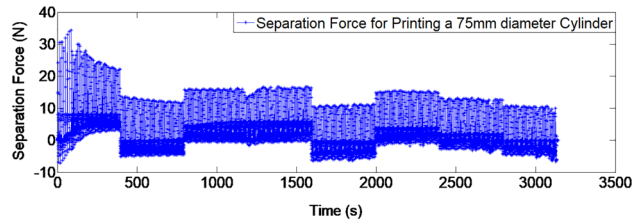


Fig. 12 Separation force for printing a 75 mm diameter cylinder using the textured constrained surface ( $\sim 520$  layers)

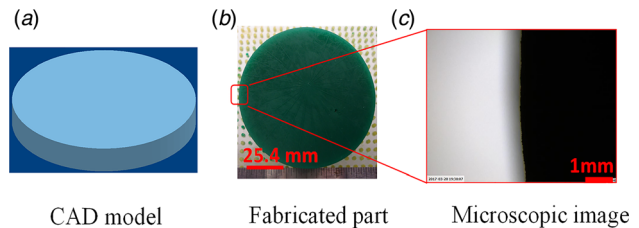


Fig. 13 A 75 mm diameter cylinder printed with the textured constrained surface

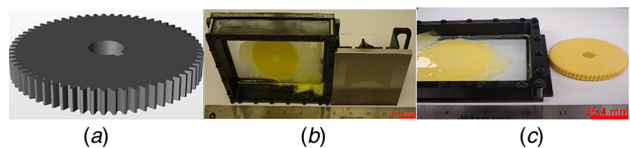


Fig. 14 (a) A CAD model of a mechanical gear, (b) failure of printing a mechanical gear in a commercial machine which uses the conventional nontextured constrained surface, and (c) comparison between the failed part printed in the commercial machine and the successfully printed part in our setup using textured constrained surface

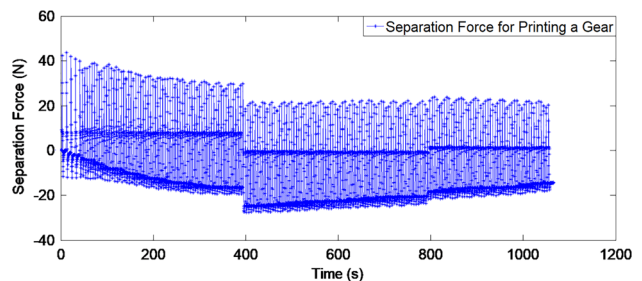


Fig. 15 Separation force for printing the mechanical gear using the textured constrained surface ( $\sim 200$  layers)

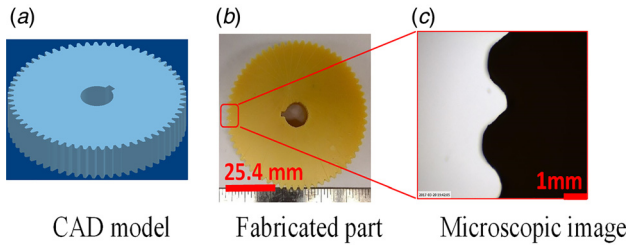


Fig. 16 A gear printed with textured constrained surface

intensity, separation speed, and environmental conditions, are all the same as those in the commercial machine. The comparison between the failure part and our successful part is given in Fig. 11(c).

The separation force for building the part with textured surface was recorded and is plotted in Fig. 12. The average separation force is  $\sim 18$  N for each layer. Besides, there is no significant increase of separation force over the manufacturing process, which is often seen in conventional constrained surface SL processes [32,33]. The CAD model, fabricated picture, and the corresponding microscopic image are shown in Fig. 13.

**4.6 Test Case 5: Fabrication of a Gear.** To further demonstrate the capability and versatility of textured constrained surface, a common mechanical gear ( $\sim 68$  mm diameter, 10 mm in height) was printed. The material used was SL600M, produced by EnvisionTEC. The part was printed using both a commercial machine with conventional constrained surface and our setup with textured surface. The microgroove width and depth of the textured surface were designed according to the theoretical model in Eq. (15), and

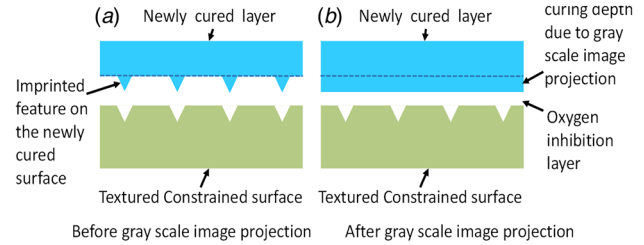


Fig. 18 Before and after gray scale image projection

manufactured to be  $100 \mu\text{m}$  and  $105 \mu\text{m}$ , respectively, with an intergroove angle of  $15^\circ$ . After printing a few layers in the commercial machine, the part was pulled down from the platform by the large separation force and adhered to the constrained surface. Debris could be observed on the metal platform and the constrained surface, as shown in Fig. 14(b).

However, with the textured surface, the gear can be successfully printed. The comparison between these two parts are given in Fig. 14(c) (scale bar: 25.4 mm). The separation force for manufacturing this gear with textured was recorded during the whole process, as plotted in Fig. 15.

The gear's CAD model, fabricated picture, cross section contour and the corresponding microscopic image are shown in Fig. 16.

**4.7 Influence of Constrained Surface Texture on Printed Surface Roughness.** Although the textured constrained surface significantly reduces the separation force and enables successful prints of objects with wide solid cross sections, the textured constrained surface brings a surface finish problem. The textures were

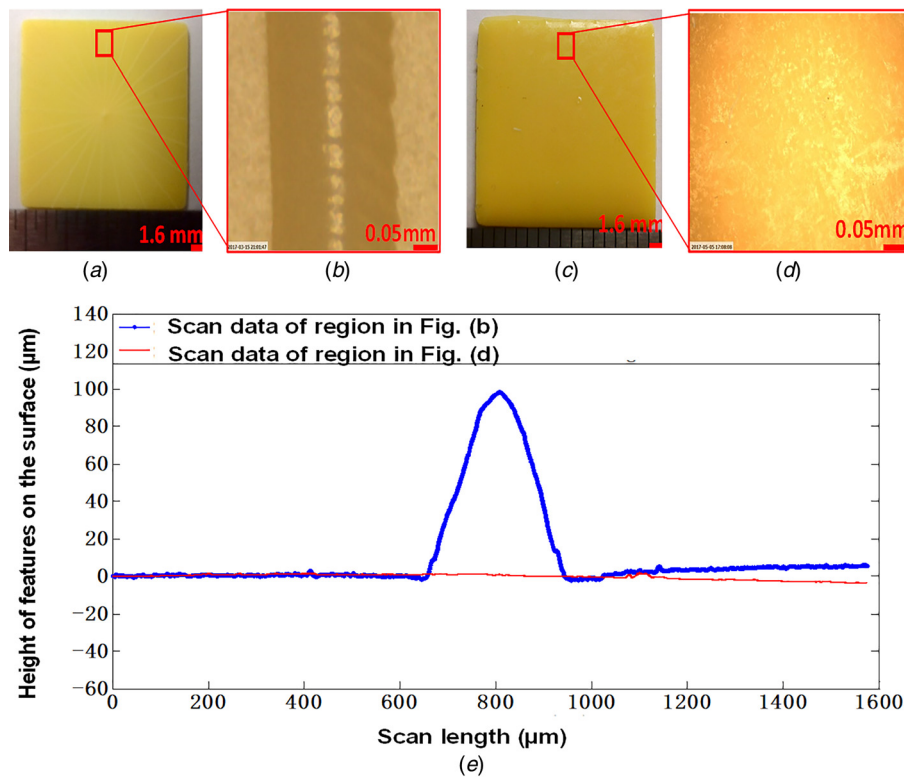


Fig. 17 Samples printed with and without gray scale images: (a) a sample printed with the conventional mask image projection method; (b) microscopic image of the imprinted texture on the sample in (a); (c) a sample printed with the proposed gray scale projection method; (d) microscopic image of the region where microtexture was imprinted; (e) Z profiles of the region of the part surface where was in contact with the microgroove on the textured constrained surface

**Table 1 Roughness measurements of parts fabricated with textured constrained surface**

Models	Ra ( $\mu\text{m}$ )	Rq ( $\mu\text{m}$ )	Rz ( $\mu\text{m}$ )
Square sample (before eliminating textures)	0.58167	0.39486	23.754
Square sample (after eliminating textures)	0.25126	0.33688	2.224
75 mm diameter cylinder	0.792	0.98444	24.055
Mechanical gear	0.27684	0.35599	25.155

imprinted on the part surface and could be observed. To better understand the effects of textured constrained surface on surface finish of printed parts, this section characterizes the part surface finish and investigate approaches to eliminate the imprinted textures.

Eight samples were manufactured using the textured PDMS constrained surface and two different resins, MakerJuice and SL600. Figure 17(a) shows a sample and Fig. 17(b) shows a microscopic image of the region that was printed by the microgroove region of the PDMS film. As shown in Fig. 17(b), the resin in the radial microsurface texture of the constrained surface was cured and printed on the surface of the square part, forming ridge shaped patterns extruding out on the surface of the printed part. A KLA-Tencor P7 stylus contact profilometer was used to characterize the imprinted textures. The profiler physically moves a probe along the surface to acquire the surface height. When the probe moved from the middle point of the left edge of the region indicated in Fig. 17(b) to the middle point of the right edge of Fig. 17(b), the corresponding profile is plotted as the blue curve in Fig. 17(e). It can be seen that the height of the printed ridge is  $\sim 100\mu\text{m}$ , which is very close to the depth of the microgroove on the PDMS surface.

To address this texture printing problem, a gray scale projection method was investigated. After curing a layer, a sliced image with gray scale values (R: 110, G: 110, B: 110) of that layer was projected [3,5]. By adjusting the gray scale values of pixels in an image, the light intensity distribution could be manipulated and thus the curing depth and width. Thus, by using a stronger light intensity in the nontextured regions and weaker intensity in the grooved regions, a bigger oxygen inhibition layer thickness will be produced in the grooved region than the nontextured region, leading to a smooth newly cured layer with uniform thickness, as illustrated in the schematic of Fig. 18.

To test the feasibility of this method, the same square sample was printed using this gray scale image method. Picture and microscopic image of the sample printed using the gray scale image method are shown in Figs. 17(c) and 17(d). The profile of the same region as in Fig. 17(b) is plotted as the red curve in Fig. 17(e). It can be seen from Figs. 17(d) and 17(e) that with the gray scale image method, the imprinted texture feature could be avoided. It showed that undesired effects of the microgroove in the PDMS constrained surface on the surface finish of printed parts could be eliminated by carefully controlling the light intensity distribution. Additionally, the surface roughness of 75 mm diameter cylinder, mechanical gear, and square samples fabricated with textured PDMS surface were measured, as listed in Table 1. It can be seen that the gray scale image method is a feasible approach to eliminating the imprinted texture and improving the surface roughness of printed parts.

## 5 Conclusions

A novel constrained surface texturing method for separation force reduction in projection stereolithography systems is developed in this study. Analytical models indicate that by modifying the constrained surface with radial microgroove patterns, the separation force during printing process could be reduced greatly. Several PDMS samples with microgroove patterns are prepared using micromilling and femtosecond laser micromachining

technologies. Separation forces during the printing process using textured constrained surfaces are measured and compared with the forces during printing process using the conventional nontextured constrained surface. Multiple parts have been built successfully with the developed projection SL process based on textured PDMS constrained surfaces. Experimental results verified the effectiveness of constrained surface texturing approach in reducing separation forces and fabricating 3D objects. Furthermore, this study demonstrated advantages of the proposed textured constrained surface in projection SL on fabricating parts with large solid cross section areas, which are very challenging or even impossible with current constrained surface projection SL technology due to over-large separation forces.

Future work will be conducted to (1) investigate a homogeneous surface texture design and further optimize it; (2) develop the gray scale image method for eliminating the texture imprinting problem for printing complicated geometries with high surface finish; and (3) study the effect of the textured constrained surface on the interlayer bonding and the mechanical strength of the printed parts.

## Acknowledgment

The authors would like to also acknowledge the Nanotechnology Core Facility of the University of Illinois at Chicago campus for training on and usage of the Bruker-Nano Model Contour GT-K Optical Profilometer.

## Funding Data

- This material is based upon work supported by the National Science Foundation (Grant No. 1563477).

## Nomenclature

- $d$  = microgroove depth
- DLP = digital light processing
- $F$  = separation force
- $L$  = channel length
- $N$  = number of microgrooves
- $P$  = pressure across the separation area
- $Q$  = liquid resin flow rate
- $R_{\text{hyd}}$  = hydraulic resistance
- SL = stereolithography
- $V$  = Z-stage moving speed
- $w$  = microgroove width
- $\alpha$  = angle of each microgroove
- $\mu$  = viscosity of the resin
- $\theta$  = microgroove radial distance
- $\nabla p$  = pressure gradient across the part

## References

- [1] Gibson, I., Rosen, D., and Stucker, B., 2014, *Additive Manufacturing Technologies: 3D Printing, Rapid Prototyping, and Direct Digital Manufacturing*, Springer, New York.
- [2] Zhou, C., Chen, Y., Yang, Z. G., and Khoshnevis, B., 2011, "Development of Multi-Material Mask-Image-Projection-Based Stereolithography for the Fabrication of Digital Materials," *Annual Solid Freeform Fabrication Symposium*, Austin, TX, pp. 65–80.
- [3] Pan, Y., Zhao, X., Zhou, C., and Chen, Y., 2012, "Smooth Surface Fabrication in Mask Projection Based Stereolithography," *J. Manuf. Processes*, **14**(4), pp. 460–470.
- [4] Zhou, C., Chen, Y., Yang, Z., and Khoshnevis, B., 2013, "Digital Material Fabrication Using Mask-Image-Projection-Based Stereolithography," *Rapid Prototyping J.*, **19**(3), pp. 153–165.
- [5] Zhou, C., and Chen, Y., 2012, "Additive Manufacturing Based on Optimized Mask Video Projection for Improved Accuracy and Resolution," *J. Manuf. Processes*, **14**(2), pp. 107–118.
- [6] Deng, D., and Chen, Y., 2015, "Origami-Based Self-Folding Structure Design and Fabrication Using Projection Based Stereolithography," *ASME J. Mech. Des.*, **137**(2), p. 021701.
- [7] Pan, Y., Patil, A., Guo, P., and Zhou, C., 2017, "A Novel Projection Based Electro-Stereolithography (PES) Process for Production of 3D Polymer-Particle Composite Objects," *Rapid Prototyping J.*, **23**(2), pp. 236–245.

- [8] Pan, Y., and Dagli, C., 2017, "Dynamic Resolution Control in a Laser Projection-Based Stereolithography System," *Rapid Prototyping J.*, **23**(1), pp. 190–200.
- [9] He, H., Pan, Y., Feinerman, A., and Xu, J., 2018, "Air-Diffusion-Channel Constrained Surface Based Stereolithography for Three-Dimensional Printing of Objects With Wide Solid Cross Sections," *ASME J. Manuf. Sci. Eng.*, **140**(6), p. 061011.
- [10] Ikuta, K., and Hirowatari, K., 1993, "Real Three Dimensional Micro Fabrication Using Stereo Lithography and Metal Molding," An Investigation of Micro Structures, Sensors, Actuators, Machines and Systems Micro Electro Mechanical Systems (MEMS'93), Fort Lauderdale, FL, Feb. 10, pp. 42–47.
- [11] He, H., Pan, Y., Xu, J., Yu, X., and Botton, V., 2016, "Effect of Surface Texturing on Separation Force in Projection Stereolithography," 11th International Conference on Micro Manufacturing (ICOMM), Irvine, CA, Mar. 29–31, p. 82.
- [12] He, H., Pan, Y., Xu, J., and Yu, X., 2017, "Effect of Constrained Surface Texturing on Separation Force in Projection Stereolithography," *Solid Freeform Fabrication Symposium*, Austin, TX, pp. 1735–1749.
- [13] Ye, H., Das, S., and Zhou, C., 2015, "Investigation of Separation Force for Bottom-Up Stereolithography Process From Mechanics Perspective," *ASME Paper No. DETC2015-47673*.
- [14] Liravi, F., Das, S., and Zhou, C., 2014, "Separation Force Analysis Based on Cohesive Delamination Model for Bottom-Up Stereolithography Using Finite Element Analysis," *25th Annual International Solid Freeform Fabrication Symposium*, Austin, TX, Aug. 4–6, pp. 1432–1451.
- [15] Huang, Y. M., and Jiang, C. P., 2005, "On-Line Force Monitoring of Platform Ascending Rapid Prototyping System," *J. Mater. Process. Technol.*, **159**(2), pp. 257–264.
- [16] Liravi, F., Das, S., and Zhou, C., 2015, "Separation Force Analysis and Prediction Based on Cohesive Element Model for Constrained-Surface Stereolithography Processes," *Comput. Aided Des.*, **69**, pp. 134–142.
- [17] Denken Corp., 1997, "SLP-4000 Solid Laser Diode Plotter," *Product Brochure*, Denken Corporation, Niigata, Japan.
- [18] Pan, Y., Zhou, C., and Chen, Y., 2012, "A Fast Mask Projection Stereolithography Process for Fabricating Digital Models in Minutes," *ASME J. Manuf. Sci. Eng.*, **134**(5), p. 051011.
- [19] Lambert, P. M., Campaigne, E. A., III, and Williams, C. B., 2013, "Design Considerations for Mask Projection Microstereolithography Systems," *Solid Freeform Fabrication Symposium*, Austin, TX, Aug. 12–14, p. 111.
- [20] John, H., and EnvisionTEC GmbH, 2007, "Apparatus and Method for the Non-Destructive Separation of Hardened Material Layers From a Flat Construction Plane," EnvisionTEC Inc., Dearborn, MI, U.S. Patent No. 7,195,472.
- [21] Srinivasan, S., Kleingartner, J. A., Gilbert, J. B., Cohen, R. E., Milne, A. J., and McKinley, G. H., 2015, "Sustainable Drag Reduction in Turbulent Taylor-Couette Flows by Depositing Sprayable Superhydrophobic Surfaces," *Phys. Rev. Lett.*, **114**(1), p. 014501.
- [22] Xu, L., 2007, "Liquid Drop Splashing on Smooth, Rough, and Textured Surfaces," *Phys. Rev. E*, **75**(5), p. 056316.
- [23] Quéré, D., Lafuma, A., and Bico, J., 2003, "Slippy and Sticky Microtextured Solids," *Nanotechnology*, **14**(10), pp. 1109–1112.
- [24] Nicolaiewsky, E. M., and Fair, J. R., 1999, "Liquid Flow Over Textured Surfaces—Part I: Contact Angles," *Ind. Eng. Chem. Res.*, **38**(1), pp. 284–291.
- [25] Bruus, H., 2007, *Theoretical Microfluidics*, Oxford University Press, Oxford, UK.
- [26] Tumbleston, J. R., Shirvanyants, D., Ermoshkin, N., Januszewicz, R., Johnson, A. R., Kelly, D., Chen, K., Pinschmidt, R., Rolland, J. P., Ermoshkin, A., and Samulski, E. T., 2015, "Continuous Liquid Interface Production of 3D Objects," *Science*, **347**(6228), pp. 1349–1352.
- [27] Dendukuri, D., Pregibon, D. C., Collins, J., Hatton, T. A., and Doyle, P. S., 2006, "Continuous-Flow Lithography for High-Throughput Microparticle Synthesis," *Nat. Mater.*, **5**(5), pp. 365–369.
- [28] Yagci, Y., Jockusch, S., and Turro, N. J., 2010, "Photoinitiated Polymerization: Advances, Challenges, and Opportunities," *Macromolecules*, **43**(15), pp. 6245–6260.
- [29] Dendukuri, D., Panda, P., Haghgooe, R., Kim, J. M., Hatton, T. A., and Doyle, P. S., 2008, "Modeling of Oxygen-Inhibited Free Radical Photopolymerization in a PDMS Microfluidic Device," *Macromolecules*, **41**(22), pp. 8547–8556.
- [30] González-Méijome, J. M., Compañ-Moreno, V., and Riande, E., 2008, "Determination of Oxygen Permeability in Soft Contact Lenses Using a Polarographic Method: Estimation of Relevant Physiological Parameters," *Ind. Eng. Chem. Res.*, **47**(10), pp. 3619–3629.
- [31] Bian, Q., Yu, X., Zhao, B., Chang, Z., and Lei, S., 2013, "Femtosecond Laser Ablation of Indium Tin-Oxide Narrow Grooves for Thin Film Solar Cells," *Opt. Laser Technol.*, **45**, pp. 395–401.
- [32] Pan, Y., He, H., Xu, J., and Feinerman, A., 2017, "Study of Separation Force in Constrained Surface Projection Stereolithography," *Rapid Prototyping J.*, **23**(2), pp. 353–361.
- [33] Zguris, Z., 2016, "How Mechanical Properties of Stereolithography 3D Prints Are Affected by UV Curing," Formlabs Inc., Somerville, MA, accessed Mar. 7, 2017, <https://formlabs.com>